# Focused Ion Beam-Induced Displacive Phase Transformation From Austenite to Martensite during Fabrication of Quenched and Partitioned Steel Micro-Pillar

**Eun Jung Seo[a,b], Lawrence Cho[c,*], Jin Kyung Kim[d], Javad Mola[e], Lijia Zhao[b], Sukjin Lee[b], Bruno C. De Cooman[a,†]**

[a]Graduate Institute of Ferrous Technology, Pohang University of Science and Technology, Pohang, 37673, South Korea

[b]Advanced Steel Processing and Products Research Center, Colorado School of Mines, Golden, CO 80401, USA

[c]National Institute of Standards and Technology, Boulder, CO 80305, USA

[d]Department of Materials Sciences & Chemical Engineering, Hanyang University, Ansan, 15588, South Korea

[e]Materials Design and Structural Integrity Laboratory, Faculty of Engineering and Computer Sciences, Osnabrück University of Applied Sciences, 49076 Osnabrück, Germany

[†]This paper is dedicated to the memory of our co-author, Bruno C. De Cooman, who passed away on August 29, 2018.

*Corresponding author. Tel: +1-303-497-6853. Email: lawrence.cho@nist.gov

## Abstract

We report evidence of a displacive phase transformation from retained austenite to martensite during preparation of quenched and partitioned steel micro-pillars by using a focused ion beam (FIB) technique. The BCC phase produced by the FIB damage was identified as martensite. The invariant-plane strain surface relief associated with the martensitic transformation was observed in the retained austenite phase immediately after a FIB scan of the surface with the $Ga^{+}$ ion beam. Use of a low acceleration voltage appears to lower the probability of the phase transformation, while a decrease of the acceleration voltage will result in an increase of the total milling time required to prepare a micro-pillar. This report addresses challenges related to the preparation of austenite micro-pillars by a conventional FIB technique.

**Keywords:** quenched and partitioned steel; micro-pillar compression; retained austenite; martensitic transformation; focused ion beam.

## Graphical Abstract

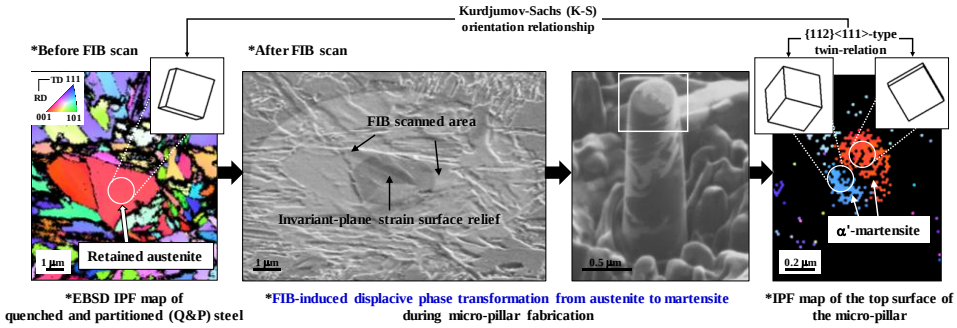

**Highlights**

- Austenite transforms to martensite during fabrication of Q&P steel micro-pillars.
- Invariant-plane strain surface relief due to the transformation is shown after a FIB scan.
- The parent austenite and product martensite had a K-S orientation relationship.
- The product BCC phase produced by the FIB damage is identified as martensite.
- A low acceleration voltage lowers the probability of the phase transformation.

## 1. Introduction

The considerable interest in third generation advanced high-strength steels (AHSSs), such as medium manganese (Mn) transformation-induced plasticity (TRIP) steels [1, 2], quenched and partitioned (Q&P) steels [3-5], and TRIP-aided bainitic ferrite (TBF) steels [6, 7], is due to their ability to achieve an attractive combination of strength and ductility with limited additions of alloying elements. In design of the AHSSs, retained austenite is known to be a key microstructural constituent required to achieve the desired mechanical properties. This is because TRIP or twinning-induced plasticity (TWIP) effect can be activated in the retained austenite, which has a pronounced influence on the strain hardening behavior [8, 9]. Similarly, metastable austenite plays an important role in the mechanical behavior of duplex stainless steels [10, 11] and some high-alloyed steels [12, 13].

Understanding of the intrinsic mechanical properties of retained austenite is of great importance for advancing design of AHSSs with improved mechanical properties. However, it is challenging to study the deformation mechanisms of the retained austenite in AHSSs because it is often fine-grained (thus size-stabilized) and influenced by the surrounding matrix. Recent studies have employed nano-indentation and micro-pillar compression tests to obtain the mechanical response of micron- and submicron-sized regions of retained austenite [14-16] or martensite/austenite (MA) constituent [17-20] in multiphase steels. The micro-pillar compression technique enables the direct analysis of the uniaxial stress-strain behavior of small volumes. Focused ion beam (FIB) milling has been used to machine micro-pillars ranging in size from submicrometers to several micrometers. Some previous works have used micro-pillar compression test data in the constitutive models for the mechanical behavior of multiphase high strength steels containing retained austenite [17, 20].

While it has been frequently shown that fabrication of a transmission electron microscopy (TEM) sample by the FIB technique may cause undesirable phase transformation due to the damage associated with a gallium (Ga) ion beam [21, 22], the possibility of an austenite-to-martensite or austenite-to-ferrite transformation during FIB-based fabrication of micro-pillars has been overlooked in previous investigations [14, 15, 17-20]. It has been shown that a mechanically-induced austenite-to-martensite transformation can result in a significant strain hardening effect [23, 24]. Mechanically-induced martensite is known to be stronger than

retained austenite [25]. Therefore, the mechanical properties measured from a micro-pillar containing retained austenite can, in fact, be flawed if the retained austenite or metastable austenite has transformed partly to mechanically-induced martensite during micro-pillar fabrication by the FIB.

The present study confirms that $Ga^+$ ion beam milling induces a transformation from carbon-enriched retained austenite to martensite during fabrication of a Q&P steel micro-pillar by the FIB technique. The phase transformation was induced by a FIB scan even under the circumstance that the retained austenite in the Q&P steel was stabilized by its high carbon (> 0.8 mass %) and Mn (4.0 mass %) contents. The present contribution discusses challenges related to fabrication of micro-pillars containing metastable austenite by means of the conventional FIB technique. The effects of the FIB parameters on the phase transformation were also investigated.

## 2. Experimental

The chemical composition of the Q&P steel used in the present study was Fe-0.41%C-4.0%Mn-1.6%Si-1.0%Cr (in mass %). The microstructure of the industrially cold-rolled sheet steel prior to quenching and partitioning processing consisted of deformed pearlite and martensite. The steel was quenched and partitioned in a dilatometer. The specimen for the dilatometry experiment had dimensions of 10 × 5 × 1.2 $mm^3$. It was heated at a rate of 10 °C/s to 850 °C and fully austenitized for 240 s at 850 °C under an argon protective atmosphere. The specimen was then initially quenched to a quenching temperature of 110 °C and held at 110 °C for 10 s, reheated to a partitioning temperature of 450 °C using a heating rate of 20 °C/s, held at 450 °C for 300 s, and finally quenched to room temperature. Both the initial and final quenching were done using helium gas to obtain a cooling rate of 50 °C/s. During the partitioning stage, carbon diffuses from the supersaturated primary martensite into the untransformed austenite, leading to the stabilization of the austenite upon cooling to room temperature. Therefore, the final microstructure of the Q&P steel consisted entirely of carbon-enriched retained austenite islands in a low-carbon primary martensite matrix. The average carbon contents of the retained austenite and martensite obtained by X-ray diffraction (XRD) and 3-dimensional atom probe tomography (3D APT) analysis were 3.6 at. % and 0.66 at. %, respectively, as was shown in a previous study [24]. Further details about the microstructural features of the alloy used in the present study can be found in a recent study by the present authors [24].

The microstructure of the steels was observed by means of field emission-scanning electron microscopy (SEM) and electron backscatter diffraction (EBSD). The samples used for the microstructural analyses were prepared by electro-chemical polishing in a solution of 5% $HClO_4$ + 95% $CH_3COOH$ in order to avoid transformation of retained austenite to mechanically-induced martensite during sample preparation.

Three micro-pillars were produced from carbon-enriched retained austenite grains of known crystallographic orientation as determined by EBSD. The micro-pillars were fabricated in a FEI Helious Nanolab 650 dual beam FIB operated at 30 kV by using the FIB-based fabrication methodology [26]. Initially, the regions of the retained austenite grains were marked by a FIB scan using 1 μs dwell time and an 80 pA beam current. Circular trenches of 40 μm diameter

were milled using a beam current of 2.5 nA to obtain 10 μm diameter posts. The outer surfaces of the 10 μm diameter pillars were milled using a lower beam current of 0.79 nA to produce about 2.5 μm diameter pillars. The pillars were then milled further to 0.6 μm diameter using a beam current in the range of 80 pA to 0.23 nA. The final milling step used a beam current of 24 pA. In each step, the milling was conducted for 3-10 min using a dwell time of 1 μs. The fabricated micro-pillars were approximately 500 nm in diameter and had a height-to-diameter aspect ratio of 3. The taper angle of the micro-pillars was approximately 4°. The EBSD analysis was performed on the top surface of the micro-pillars. The EBSD results were compared with the theoretical pole figures of austenite and martensite variants, simulated using the Python-based software, GenOVa [27]. A TEM sample was taken from one of the three micro-pillars using the FIB technique in a dual beam FIB. The TEM observations were conducted in a FE-TEM operated at 200 kV. In order to investigate the effects of the FIB parameters on the FIB-induced phase transformation, a second set of FIB milling tests was conducted. Different regions of retained austenite grains were exposed to FIB scan for a milling time of 1 s under different FIB conditions (acceleration voltage and beam current). The parameters used for the FIB milling are listed in Table 1. The milling pattern with dimensions of 0.5 μm x 2 μm was used. EBSD was used to analyze the phase change prior to and after the FIB milling.

## 3. Results and discussion

Fig. 1 clearly shows that carbon-enriched retained austenite in the Q&P steel transformed to martensite during the micro-pillar fabrication by the FIB. The micro-pillar was prepared in an area of a carbon-enriched retained austenite grain, as shown in Figs. 1(a) to (d). The selected retained austenite grain had a relatively coarse grain size, approximately 4 μm. An invariant-plane strain surface relief associated with the martensitic transformation [28] was clearly observed in the retained austenite phase immediately after a scan of the surface with the $Ga^+$ ion beam (Figs. 1(e) and (f)). This instantaneous phase transformation is likely associated with the fact that outer part of the retained austenite grain was affected by the FIB scan, as indicated by the arrows in Fig. 1(e). It should be noted that the center area of the retained austenite grain, which was not exposed directly to the FIB, was also transformed due to the $Ga^+$ ion beam scan. After the preparation of the micro-pillar (Figs. 1(g) and (h)), the top surface of the micro-pillar was analyzed by means of EBSD (Figs. 1(i) and (j)). The crystal structure of the product phase was clearly identified as BCC by the EBSD analysis (Fig. 1(j)).

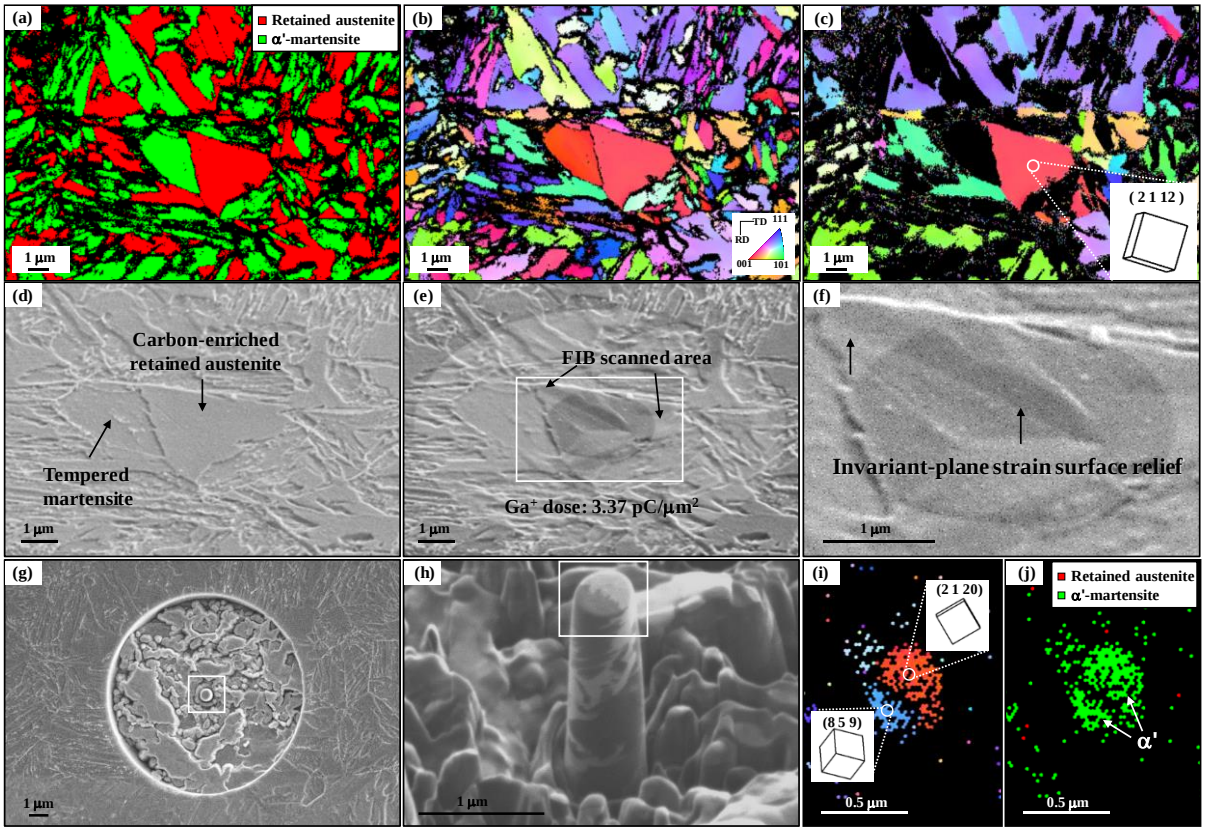

Fig. 1 Preparation of a micro-pillar from a bulky-type, coarse grain (≈ 4 μm) of the carbon-enriched retained austenite in an Fe-0.4C-4.0Mn-1.6Si-1.0Cr Q&P steel. (a) EBSD phase map for the low carbon primary martensite (green) and the carbon-enriched retained austenite (red). (b) EBSD IPF map for the low carbon primary martensite (BCC) and the carbon-enriched retained austenite (FCC) in the Q&P steel. (c) EBSD inverse pole figure (IPF) map for the retained austenite (FCC). (d) Corresponding SEM micrograph taken at a tilt angle of 52°. (e) SEM micrograph taken at a tilt angle of 52° after a $Ga^+$ ion beam scan using 1 μs dwell time, 1 s milling time, and 80 pA beam current at 30 kV. (f) Enlargement of the austenite grain surface indicated by the rectangle in (e) showing the surface relief due to the invariant-plane strain associated with the martensitic transformation. (g) SEM micrograph of the FIB micro-pillar fabricated in the retained austenite grain indicated by the rectangle in (e). (h) FIB image of the micro-pillar showing the grain boundary at the top surface of the micro-pillar. (i) EBSD IPF map of the micro-pillar corresponding to the area indicated by rectangle in (h). (j) EBSD phase map for BCC (green) and the FCC (red) phases showing that the retained austenite grain transformed to martensite during micro-pillar preparation. Two martensite variants are visible in (h) to (j). Colors in the IPF maps of (a), (b), and (i) denote crystal directions parallel to the pillar height according to the color scheme represented by the stereographic triangle in (b).

Fig. 2 shows the crystallographic orientation data of the top surface of the Q&P steel micro-pillar shown in Fig 1, revealing orientation relationships between the parent retained austenite before the FIB scan and product BCC phase, namely two martensite variants, formed due to the $Ga^+$ ion beam scan. Fig. 2(b) shows an experimental <001>γ pole figure of the retained austenite and <111>α' pole figures of the product martensite variants, obtained by EBSD analysis. Using the GenOVa program [27], the <001>γ pole figure of austenite was adjusted to match the experimental <001>γ pole figure. Subsequently, theoretical <111>α' pole positions corresponding to the austenite orientation were calculated assuming a Kurdjumov-Sachs (K-S) orientation relationship. The calculated pole figures for two of the 24 K-S variants matching the experimental results are shown in Fig. 2(c). A comparison of the <001>γ and <111>α' pole figures obtained by EBSD (Fig. 2(b)) with the simulated results (Fig. 2(c)) confirms the K-S orientation relationship between the parent retained austenite and product martensite variants. In addition, the two neighboring martensite variants had a single <111> common axis (Fig. 2(b)) and three <112> common axes lying on the plane trace for the <111> common axis (Fig. 2(d)). The misorientation angle between these two martensite variants were approximately 60 ° (Fig. 2(e)). These results indicate that the two martensite variants were {112}<111>-type twin-related [29].

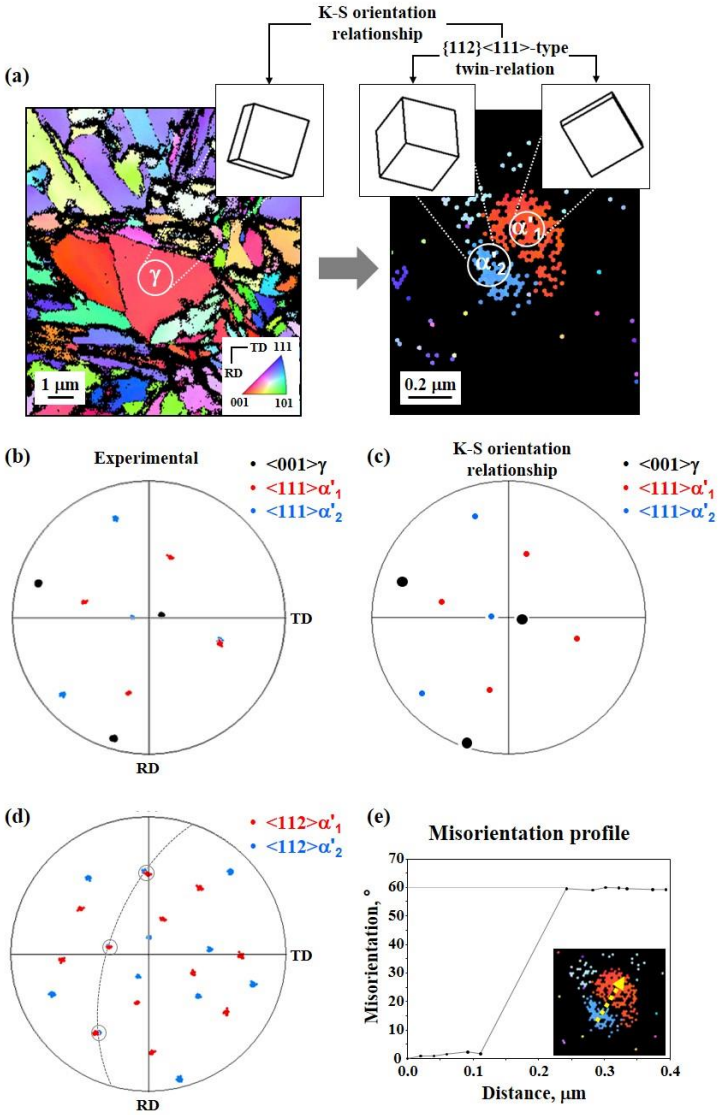


Fig. 2 Crystallographic orientation data of the top surface of the Q&P steel micro-pillar shown in Fig. 1 before the FIB scanning and after the micro-pillar fabrication. (a) EBSD IPF maps for the retained austenite (FCC) and martensite (BCC) and three-dimensional crystal orientations, represented by unit cells, for the parent retained austenite (left) and two product martensite variants formed due to the $Ga^+$ ion beam damage (right). (b) <001>γ pole figure of the retained austenite and <111>α' pole figures of the product martensite variants. (c) Simulation of the theoretical <111>α' pole figures for two of the 24 possible K-S variants closely matching the experimental pole figures. (d) <112>α' pole figures for the two martensite variants showing the coincidence of the three <112>α' poles (marked by grey circles) lying on the plane trace for the common <111>α' axis. (e) Misorientation profile of the investigated twinned martensite, taken across the twin boundary, as indicated by a dashed arrow in the inset

The FIB-induced phase transformation during micro-pillar fabrication was observed for all three micro-pillars in the present study. Fig. 3 shows another example of the retained austenite-

to-martensite transformation during the micro-pillar fabrication. The selected retained austenite grain had a grain size of approximately 2 μm. Supported by the absence of surface relief, the retained austenite did not immediately transform to martensite after a $Ga^+$ ion beam scan of the surface (Figs. 3(c) and (d)). Fig. 3(d) shows that the retained austenite grain was smaller than the inner diameter (3 μm) of the ring pattern of the FIB scanned area, indicating that this retained austenite grain was less influenced by the $Ga^+$ ion beam compared to the coarse retained austenite grain shown in Fig. 1. However, despite the smaller grain size and thus likely increased austenite stability, the retained austenite grain also transformed to martensite in the later stages of the micro-pillar fabrication process, as shown in the EBSD results in Figs. 3(f) and (g). The K-S orientation relationship existed between the parent retained austenite and product martensite variants (Supplementary Fig. S1), similar to the first example of the micro-pillar fabrication shown in Figs. 1 and 2. Furthermore, the observed martensite variants were twin-related (Supplementary Fig. S1).

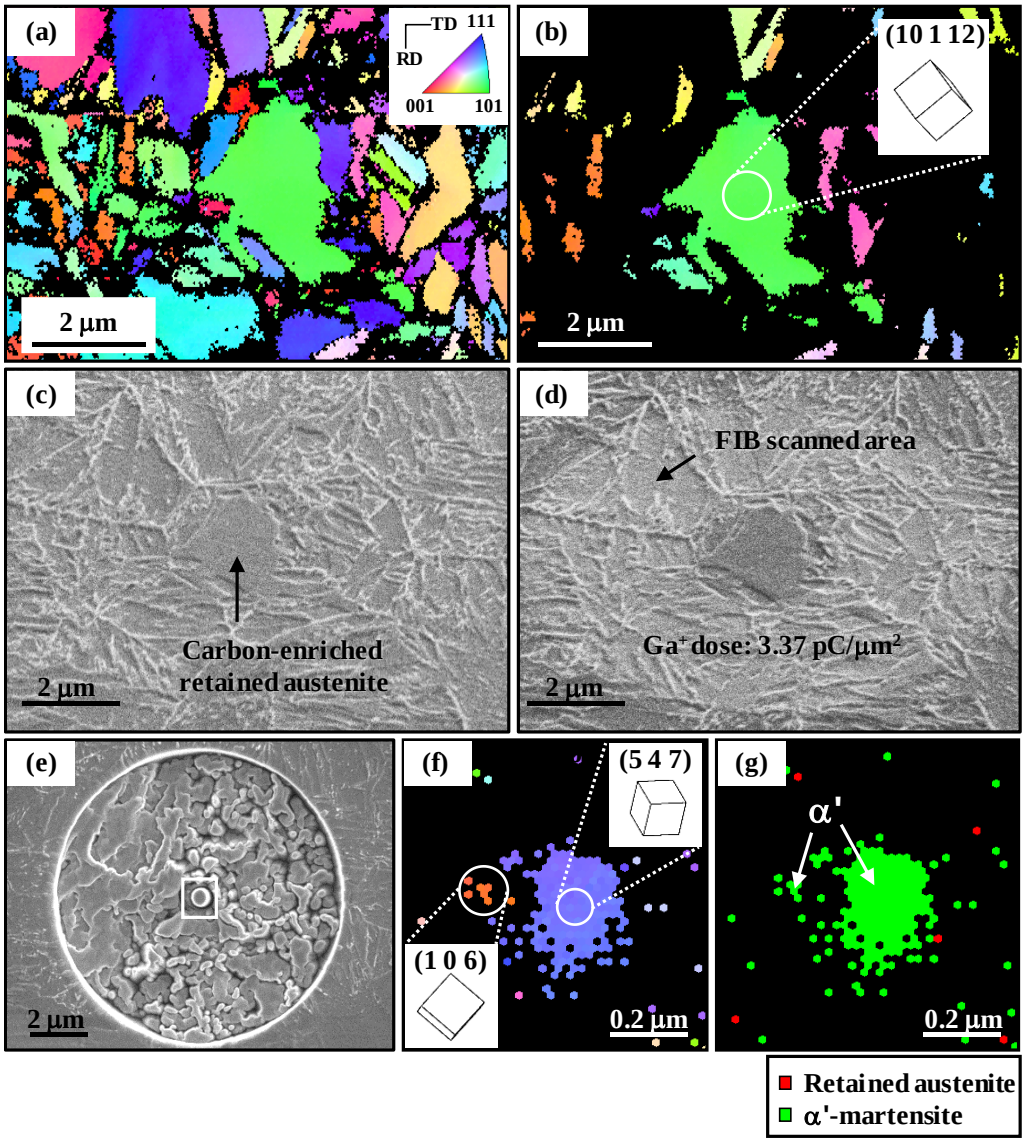


Fig. 3 Preparation of a micro-pillar from a carbon-enriched retained austenite grain (a grain diameter of approximately 2 μm). (a) EBSD IPF map of the Q&P steel microstructure. (b) EBSD orientation map for retained austenite (FCC phase). (c) Corresponding SEM micrograph taken at a tilt angle of 52°. (d) SEM micrograph taken at a tilt angle of 52° after a $Ga^+$ ion beam scan using 1 μs dwell time, 1 s milling time, and 80 pA beam current at 30 kV, showing no surface relief due to the martensitic transformation. (e) SEM micrograph of the FIB micro-pillar fabricated from the center of the retained austenite grain shown in (c) and (d). (f) EBSD orientation map of the top surface of the micro-pillar, corresponding to the area indicated by the rectangle in (e). (g) EBSD phase map for BCC (green) and the FCC (red) phases showing that the retained austenite grain transformed to martensite during micro-pillar preparation. Colors in the IPF maps of (a), (b), and (f) denote crystal directions parallel to the pillar height according to the color scheme represented by the stereographic triangle in (a).

Fig. 4 shows SEM and TEM micrographs of a micro-pillar that was prepared in an area of carbon-enriched retained austenite region. Note that the layer covering the surface of the micro-

pillar shown in Fig. 4(c) is a Pt coating layer which was deposited to protect the surface during the TEM sample preparation by the FIB lift-out technique. The cross-sectional TEM micrographs in Figs. 4(d) and (e) clearly show lath martensitic microstructure near the top surface of the micro-pillar. The selected area diffraction pattern in Fig. 4(f) indicates the BCC crystal structure of the observed martensite, again confirming the occurrence of transformation from retained austenite to martensite due to the $Ga^+$ ion beam. It should be noted that the ring patterns and extra spots in the diffraction pattern of Fig. 4(f), taken near the top surface of the micro-pillar, originated from the Pt coating layer. {112}<111>-type twinned martensite was observed near the top surface of the micro-pillar, as can be evidenced by the characteristic twin spots in the diffraction pattern of the martensite shown in Fig. 4(g). The observed twinned martensite was likely originated from the carbon-enriched retained austenite, considering the fact that twinned martensite is more frequently observed in as-quenched high carbon steels as compared to as-quenched low carbon steels [30, 31].

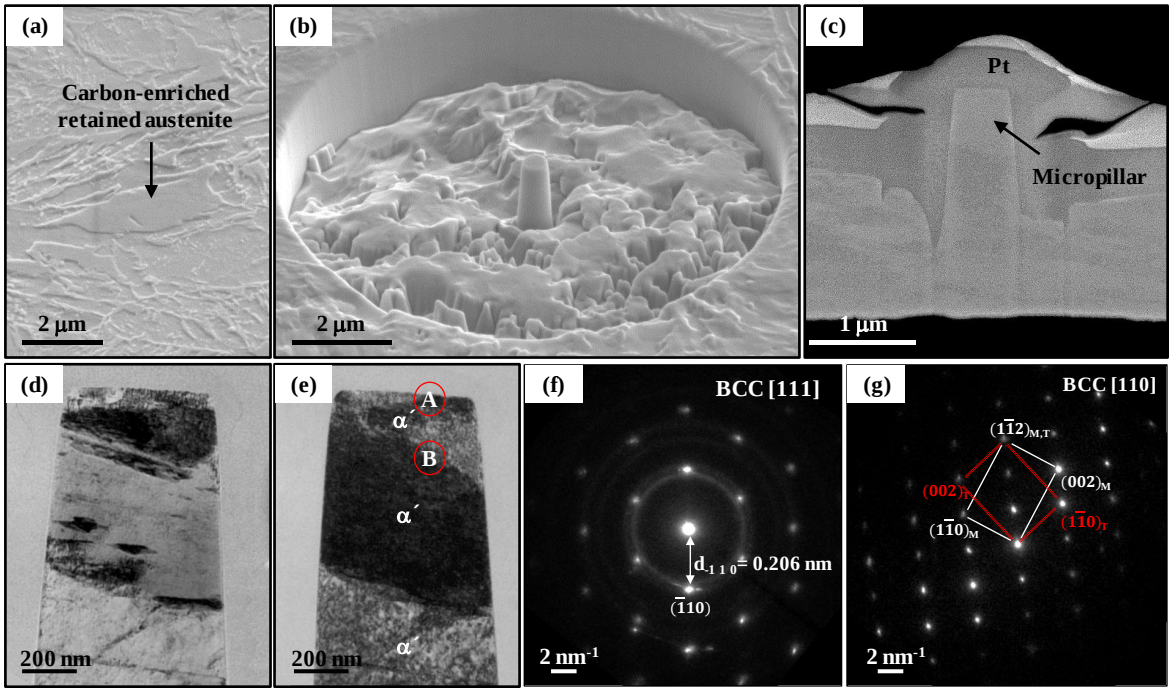


Fig. 4(a) SEM micrograph, taken at a tilt angle of 52°, of a carbon-enriched retained austenite grain in the Q&P steel microstructure. (b) SEM micrograph of the FIB micro-pillar fabricated from the retained austenite grain indicated by an arrow in (a). (c) Cross-sectional SEM image of the TEM specimen of the undeformed micro-pillar. (d,e) Cross-sectional TEM micrographs showing the lath martensitic microstructure at the top of the micro-pillar, confirming that the carbon-enriched retained austenite transformed to α'-martensite due to the $Ga^+$ ion beam

milling. (f) Selected area diffraction pattern of the martensite corresponding to the area labeled A in (e). (g) Selected area diffraction pattern of the twinned martensite corresponding to the area labeled B in (e).

Knipling *et al.* [32] reported that FIB milling resulted in the austenite-to-ferrite transformation in commercial stainless steels. Basa *et al.* [33] reported a very similar FIB-induced phase transformation in the highly stable austenite phase of a super duplex stainless steel. Similarly, Seo *et al*. [16] observed FIB-induced austenite-to-ferrite transformation in a medium Mn austenitic steel (Fe-1.2C-7.0Mn in mass %). Basa *et al.* [33] concluded that the product BCC phase was not formed by martensitic transformation since the invariant-plane strain characteristic of a martensitic transformation did not occur. In contrast, as supported by the following observations, the product BCC phase observed in the present study can be clearly identified as martensite. First, an invariant-plane strain surface relief associated with the martensitic transformation was clearly observed in the first example of the micro-pillar fabrication in the present study (Fig. 1). Second, this transformation took place immediately after the retained austenite grain was exposed to a FIB scan with a total milling time of 1 s (Fig. 1) and for materials with high thermal conductivity, the FIB-induced heating is negligible for the most beam conditions [34, 35]. Therefore, phase transformation by diffusional mechanism is unlikely. Furthermore, the {112}<111>-type twin-related martensite variants were frequently observed near the top surface of the micro-pillar (Figs. 2, 4, and 5 and Supplementary Fig. S1). Additionally, the TEM results displayed the lath martensitic microstructure near the top surface of the micro-pillar (Fig. 4).

The effects of the FIB milling conditions on the FIB-induced austenite-to-martensite transformation are shown in Table 1 and Fig. 5. As the purpose of this investigation was to analyze the instantaneous phase transformation caused by a FIB scan, a relatively short milling time of 1 s was used in all cases. A FIB snapshot image, often used to spot a region of interest prior to the actual FIB milling, was not taken in the present case. After the FIB scanning using a relatively low beam current of 24 pA at 30 kV (Figs. 5(a) and (d)), part of the retained austenite grain transformed to twinned martensite. Like the example of the micro-pillar fabrication shown in Fig. 1, the area of the retained austenite grain that was not exposed directly to the FIB scan was also transformed to martensite. The FIB-induced martensitic transformation was noted even after the FIB milling using a lower acceleration voltage of 8 kV in combination of a 110 pA beam current (Figs. 5(b) and (e)). The martensitic lath formed near

the FIB scanned area is visible in the EBSD phase map and IPF map of Fig. 5(e). When using 68 pA beam current and 5 kV acceleration voltage, no evidence of the phase transformation was observed near the FIB scanned area in the retained austenite grains, which suggests that the use of a lower acceleration voltage could reduce the FIB damage, at least for a similar $Ga^+$ dose amount (Figs. 5(d) and (f)). It should be pointed out, however, that a decrease of acceleration voltage will lead to a significant increase of the total milling time required to prepare a micro-pillar, and the milling time may affect the occurrence of the FIB-induced phase transformation. Moreover, the severity of the FIB damage may also depends on other factors such as grain orientation and ion incident angle, which are known to influence the amount of $Ga^+$ implantation [36]. Further investigation will be needed to determine whether the above-mentioned factors, i.e. milling time, grain orientation, and ion incident angle, influence the stability of retained austenite.

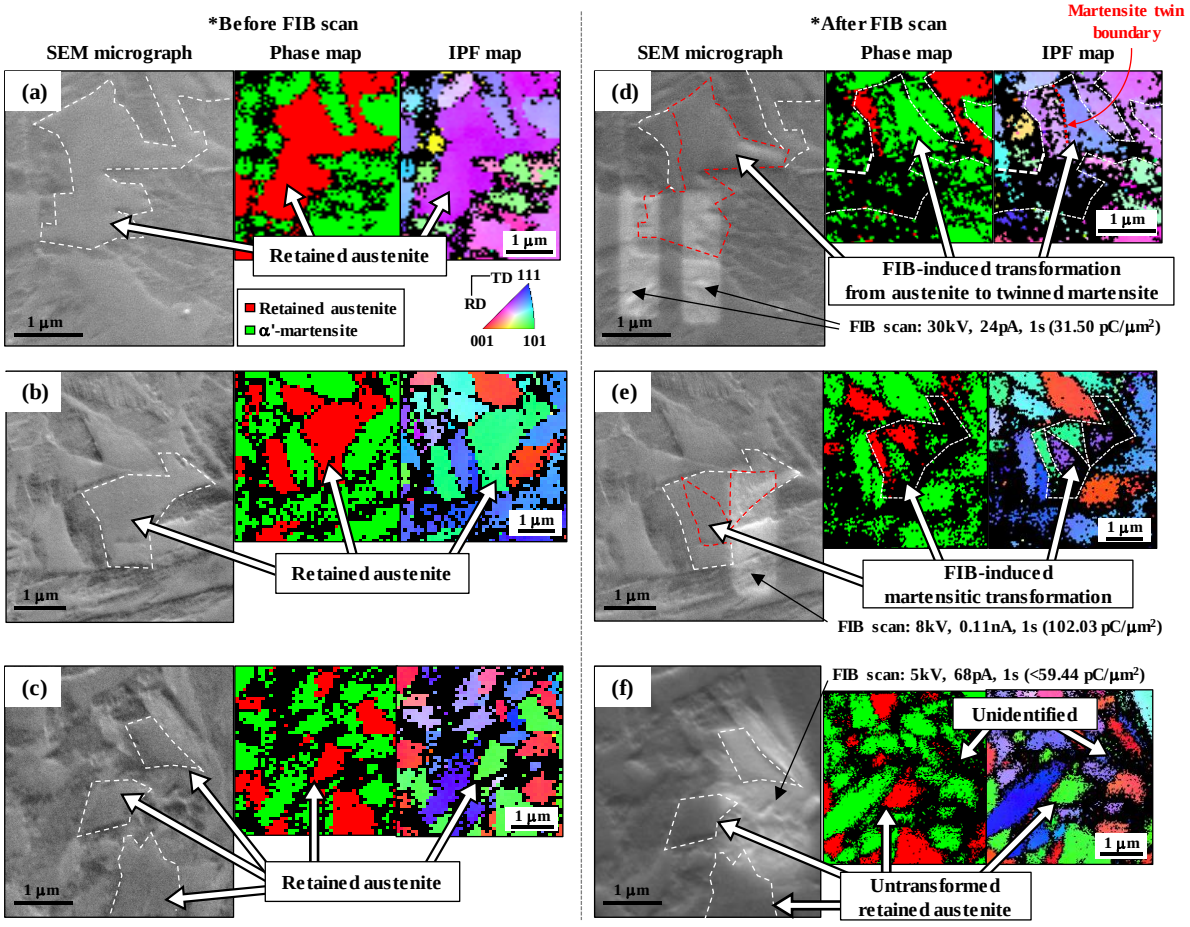


Fig. 5 Representative SEM micrographs, EBSD phase maps, and IPF maps of carbon-enriched retained austenite grains in the Q&P steel microstructure before ((a) to (c)) and after the FIB scanning using different FIB milling conditions ((d) to (f)). In all cases, the dwell time and total

milling time were 1 μs and 1 s, respectively.

As to the mechanism of the ion beam-induced phase transformation, many previous works focused on the effect of physical damage induced by the ion implantation [37-42]. In a recent study of Knipling *et al.* [32], the authors argued that the austenite-to-ferrite transformation observed in stainless steels was chemically-induced, i.e. the transformation was due to the local enrichment of Ga, which is a strong ferrite stabilizer. On the other hand, Babu *et al.* [36] reported that in addition to the local Ga enrichment, the strain associated with the ion implantation also promoted the FIB-induced austenite-to-ferrite transformation in 316L austenitic stainless steel. It is interpreted that the FIB-induced austenite-to-martensite transformation noted for the investigated Q&P steel, reported herein, was driven by the stress/strain associated with the ion implantation, rather than by a diffusional mechanism.

It has been suggested that the mechanism of the phase transformation during the FIB microfabrication depends on the austenite stability [16, 36]. In the case of the highly stable austenite in the medium Mn austenitic steel [16] and the super duplex stainless steel [36], the transformation was mainly chemically-driven. That is, during the $Ga^+$ ion implantation, the austenite is destabilized due to an increase in the concentration of the ferrite-stabilizing Ga. Once a critical Ga content is reached, the austenite spontaneously transforms to ferrite. On the other hand, if the austenite is metastable or less stable, the phase transformation may be triggered mainly by the stress/strain generated by the ion implantation. As the contents of carbon and Mn, which are austenite stabilizers, were relatively low in the investigated Q&P steel (Fe-0.4C-4.0Mn-1.6Si-1.0Cr in mass %), the stability of the retained austenite in this steel was clearly much lower than in the medium Mn austenitic steel [16] and the duplex stainless steel [36]. Therefore, the FIB-induced martensitic transformation, driven mechanically, observed for the investigated Q&P steel is likely associated with the relatively low stability of the retained austenite.

It may be argued that the effects of the FIB-induced phase change may be negligible considering the large errors associated with the nature of mechanical testing on the micro-scale. It is, however, emphasized that when the austenite-to-martensite transformation takes place due to the ion-beam damage, the volume of the transformed region is much larger, and thus its impacts on the measured mechanical properties can be significant, as compared to the FIB-

induced austenite-to-ferrite transformation. Specifically, the martensitic lath nucleated from the area directly exposed to the FIB can grow a distance of several micrometers (Figs. 1 and 5), while the thickness of the FIB-induced ferrite layer is generally limited to several tens of nanometers depending on the FIB fabrication conditions [16, 36].

## 4. Conclusions

In summary, we report that FIB milling induced an austenite-to-martensite transformation during fabrication of Q&P steel micro-pillars. In the present study, the BCC phase produced by the FIB damage was identified as martensite. The observed orientation relationship between the parent retained austenite and product martensite variants was close to the K-S orientation relationship. The transformation product, i.e. untempered high carbon martensite, in the retained austenite micro-pillar fabricated by FIB may critically alter the mechanical properties of the micro-pillar. In order to reduce the unfavorable influence of the FIB-induced phase transformation near the outer surfaces of a metastable austenite micro-pillar, it is suggested to fabricate a micro-pillar with relatively large dimensions. Furthermore, use of a low acceleration voltage appears to lower the probability of the phase transformation, while a decrease of the acceleration voltage will result in an increase of the total milling time required to prepare a micro-pillar. It should also be noted that even a single FIB snapshot might damage the surface area and trigger the martensitic transformation.

## Acknowledgements

The authors gratefully acknowledge the support of the POSCO Technical Research Laboratories, Gwangyang, South Korea, for providing the materials used for this investigation. We would also like to thank Cyril Cayron from the Laboratory of Thermomechanical Metallurgy (LMTM), Ecole Polytechnique Fédérale de Lausanne (EPFL), Switzerland, for his support with the crystallographic orientation simulations using GenOVa. We are also grateful to Chang-yeol Oh at National Institute for Nanomaterials Technology (NINT), Pohang, South Korea for helpful discussions. Commercial equipment, instruments, or materials are identified only in order to adequately specify certain procedures. In no case does such identification imply recommendation or endorsement by the National Institute of Standards and Technology, nor does it imply that the products identified are necessarily the best available for the purpose.

## References


[1] R. Zhang, W.Q. Cao, Z.J. Peng, J. Shi, H. Dong, C.X. Huang, Mater. Sci. Eng. A 583 (2013) 84-88.

[2] S. Lee, S. Shin, M. Kwon, K. Lee, B.C. De Cooman, Metall. Mater. Trans. A 48(4) (2017) 1678-1700.

[3] E.J. Seo, L. Cho, B.C. De Cooman, Metall. Mater. Trans. A 45(9) (2014) 4022-4037.

[4] L. Liu, B.B. He, G.J. Cheng, H.W. Yen, M.X. Huang, Scr. Mater. 150 (2018) 1-6.

[5] E.J. Seo, L. Cho, B.C. De Cooman, Metall. Mater. Trans. A 46(1) (2015) 27-31.

[6] K.-i. Sugimoto, M. Tsunezawa, T. Hojo, S. Ikeda, ISIJ Int. 44(9) (2004) 1608-1614.

[7] K. Hausmann, D. Krizan, K. Spiradek-Hahn, A. Pichler, E. Werner, Mater. Sci. Eng. A 588 (2013) 142-150.

[8] S. Lee, Y. Estrin, B.C. De Cooman, Metall. Mater. Trans. A 44(7) (2013) 3136-3146.

[9] E.J. Seo, L. Cho, Y. Estrin, B.C. De Cooman, Acta Mater. 113 (2016) 124-139.

[10] C. Herrera, D. Ponge, D. Raabe, Acta Mater. 59(11) (2011) 4653-4664.

[11] D. Fahr, Metall. Trans. 2(7) (1971) 1883-1892.

[12] A. Weidner, S. Martin, V. Klemm, U. Martin, H. Biermann, Scr. Mater. 64(6) (2011) 513-516.

[13] T.-H. Lee, C.-S. Oh, S.-J. Kim, Scr. Mater. 58(2) (2008) 110-113.

[14] E.-Y. Guo, H.-X. Xie, S.S. Singh, A. Kirubanandham, T. Jing, N. Chawla, Mater. Sci. Eng. A 598 (2014) 98-105.

[15] O.G. Nimaga, G.J. Cheng, H.W. Yen, M.X. Huang, Scr. Mater. 137 (2017) 64-68.

[16] E.J. Seo, J.K. Kim, L. Cho, J. Mola, C.Y. Oh, B.C. De Cooman, Acta Mater. 135 (2017) 112-123.

[17] A. Srivastava, H. Ghassemi-Armaki, H. Sung, P. Chen, S. Kumar, A.F. Bower, J. Mech. Phys. Solids 78 (2015) 46-69.

[18] J.J. Roa, J.M. Wheeler, T. Trifonov, G. Fargas, A. Mateo, J. Michler, E. Jiménez-Piqué, Mater. Sci. Eng. A 647 (2015) 51-57.

[19] H. Jirková, B. Mašek, M.F.X. Wagner, D. Langmajerová, L. Kučerová, R. Treml, D. Kiener, J. Alloy. Compd. 615 (2014) S163-S168.

[20] B.R.S. Rogne, C. Thaulow, A. Barnoush, Metall. Mater. Trans. A 45(4) (2014) 1996-2003.

[21] L.A. Giannuzzi, F.A. Stevie, Micron 30(3) (1999) 197-204.

[22] J. Mayer, L.A. Giannuzzi, T. Kamino, J. Michael, MRS bulletin 32(5) (2007) 400-407.

[23] T.-H. Ahn, C.-S. Oh, D. Kim, K. Oh, H. Bei, E.P. George, H. Han, Scr. Mater. 63(5) (2010) 540-543.
[24] E.J. Seo, L. Cho, J.K. Kim, J. Mola, L. Zhao, B.C. De Cooman, Mater. Sci. Eng. A 740-741 (2018) 439-444.
[25] A. Weidner, U.D. Hangen, H. Biermann, Philos. Mag. Lett. 94(8) (2014) 522-530.
[26] M.D. Uchic, D.M. Dimiduk, Mater. Sci. Eng. A 400-401 (2005) 268-278.
[27] C. Cayron, J. Appl. Crystallogr. 40(6) (2007) 1183-1188.
[28] Z.-G. Yang, H.-S. Fang, J.-J. Wang, C.-M. Li, Y.-K. Zheng, Phys. Rev. B 52(11) (1995) 7879.
[29] J. Xie, H. Fu, Z. Zhang, Y. Jiang, Mater. Sci. Eng. A 538 (2012) 315-319.
[30] G. Krauss, Mater. Sci. Eng. A A273-275 (1999) 40-57.
[31] G. Krauss, A.R. Marder, Metall. Trans. 2(9) (1971) 2343-2357.
[32] K.E. Knipling, D.J. Rowenhorst, R.W. Fonda, G. Spanos, Mater. Charact. 61(1) (2010) 1-6.
[33] A. Basa, C. Thaulow, A. Barnoush, Metall. Mater. Trans. A 45(3) (2014) 1189-1198.
[34] C.A. Volkert, A.M. Minor, MRS bulletin 32(5) (2007) 389-399.
[35] N. Bassim, B. De Gregorio, A. Kilcoyne, K. Scott, T. Chou, S. Wirick, G. Cody, R. Stroud, J. Microsc. 245(3) (2012) 288-301.
[36] R.P. Babu, S. Irukuvarghula, A. Harte, M. Preuss, Acta Mater. 120 (2016) 391-402.
[37] D. Gustiono, N. Sakaguchi, T. Shibayama, H. Kinoshita, H. Takahashi, Mater. Trans. 45(1) (2004) 65-68.
[38] G. Xie, M. Song, K. Mitsuishi, K. Furuya, J. Nucl. Mater. 281(1) (2000) 80-83.
[39] S. Raud, H. Garem, A. Naudon, J.P. Villain, P. Moine, Mater. Sci. Eng. A 115 (1989) 245-251.
[40] T. Laursen, J.L. Whitton, G. Dearnaley, Mater. Sci. Eng. A 116 (1989) 97-101.
[41] E. Johnson, U. Littmark, A. Johansen, C. Christodoulides, Philos. Mag. A 45(5) (1982) 803-821.
[42] E. Johnson, T. Wohlenberg, W.A. Grant, Phase Transit. 1(1) (1979) 23-33.

Table 1. Parameters used for the FIB milling and occurrence of FIB-induced austenite-to-martensite transformation.

| Acceleration voltage (kV) | Beam current (pA) | Dwell time (μs) | Milling time (s) | $Ga^+$ dose (pC/μm$^2$) | Number of the tested austenite grains | Number of the transformed grains after the FIB scan |
|---|---|---|---|---|---|---|
| 30 | 80 | 1 | 1 | 313.40 | 3 | 3 |
| | 24 | 1 | 1 | 31.50 | 3 | 3 |
| 8 | 110 | 1 | 1 | 102.03 | 3 | 3 |
| 5 | 68 | 1 | 1 | < 59.34 | 3 | 0 |

**Figure captions**

Fig. 1 Preparation of a micro-pillar from a bulky-type, coarse grain (≈ 4 μm) of the carbon-enriched retained austenite in an Fe-0.4C-4.0Mn-1.6Si-1.0Cr Q&P steel. (a) EBSD phase map for the low carbon primary martensite (green) and the carbon-enriched retained austenite (red). (b) EBSD IPF map for the low carbon primary martensite (BCC) and the carbon-enriched retained austenite (FCC) in the Q&P steel. (c) EBSD inverse pole figure (IPF) map for the retained austenite (FCC). (d) Corresponding SEM micrograph taken at a tilt angle of 52°. (e) SEM micrograph taken at a tilt angle of 52° after a $Ga^+$ ion beam scan using 1 μs dwell time, 1 s milling time, and 80 pA beam current at 30 kV. (f) Enlargement of the austenite grain surface indicated by the rectangle in (e) showing the surface relief due to the invariant-plane strain associated with the martensitic transformation. (g) SEM micrograph of the FIB micro-pillar fabricated in the retained austenite grain indicated by the rectangle in (e). (h) FIB image of the micro-pillar showing the grain boundary at the top surface of the micro-pillar. (i) EBSD IPF map of the micro-pillar corresponding to the area indicated by rectangle in (h). (j) EBSD phase map for BCC (green) and the FCC (red) phases showing that the retained austenite grain transformed to martensite during micro-pillar preparation. Two martensite variants are visible in (h) to (j). Colors in the IPF maps of (a), (b), and (i) denote crystal directions parallel to the pillar height according to the color scheme represented by the stereographic triangle in (b).

Fig. 2 Crystallographic orientation data of the top surface of the Q&P steel micro-pillar shown in Fig. 1 before the FIB scanning and after the micro-pillar fabrication. (a) EBSD IPF maps for the retained austenite (FCC) and martensite (BCC) and three-dimensional crystal orientations, represented by unit cells, for the parent retained austenite (left) and two product martensite variants formed due to the $Ga^+$ ion beam damage (right). (b) <001>γ pole figure of the retained austenite and <111>α' pole figures of the product martensite variants. (c) Simulation of the theoretical <111>α' pole figures for two of the 24 possible K-S variants closely matching the experimental pole figures. (d) <112>α' pole figures for the two martensite variants showing the coincidence of the three <112>α' poles (marked by grey circles) lying on the plane trace for the common <111>α' axis. (e) Misorientation profile of the investigated twinned martensite, taken across the twin boundary, as indicated by a dashed arrow in the inset

Fig. 3 Preparation of a micro-pillar from a carbon-enriched retained austenite grain (a grain

diameter of approximately 2 μm). (a) EBSD IPF map of the Q&P steel microstructure. (b) EBSD orientation map for retained austenite (FCC phase). (c) Corresponding SEM micrograph taken at a tilt angle of 52°. (d) SEM micrograph taken at a tilt angle of 52° after a $Ga^+$ ion beam scan using 1 μs dwell time, 1 s milling time, and 80 pA beam current at 30 kV, showing no surface relief due to the martensitic transformation. (e) SEM micrograph of the FIB micro-pillar fabricated from the center of the retained austenite grain shown in (c) and (d). (f) EBSD orientation map of the top surface of the micro-pillar, corresponding to the area indicated by the rectangle in (e). (g) EBSD phase map for BCC (green) and the FCC (red) phases showing that the retained austenite grain transformed to martensite during micro-pillar preparation. Colors in the IPF maps of (a), (b), and (f) denote crystal directions parallel to the pillar height according to the color scheme represented by the stereographic triangle in (a).

Fig. 4(a) SEM micrograph, taken at a tilt angle of 52°, of a carbon-enriched retained austenite grain in the Q&P steel microstructure. (b) SEM micrograph of the FIB micro-pillar fabricated from the retained austenite grain indicated by an arrow in (a). (c) Cross-sectional SEM image of the TEM specimen of the undeformed micro-pillar. (d,e) Cross-sectional TEM micrographs showing the lath martensitic microstructure at the top of the micro-pillar, confirming that the carbon-enriched retained austenite transformed to α'-martensite due to the $Ga^+$ ion beam milling. (f) Selected area diffraction pattern of the martensite corresponding to the area labeled A in (e). (g) Selected area diffraction pattern of the twinned martensite corresponding to the area labeled B in (e).

Fig. 5 Representative SEM micrographs, EBSD phase maps, and IPF maps of carbon-enriched retained austenite grains in the Q&P steel microstructure before ((a) to (c)) and after the FIB scanning using different FIB milling conditions ((d) to (f)). In all cases, the dwell time and total milling time were 1 μs and 1 s, respectively.

**Supplementary Figure**

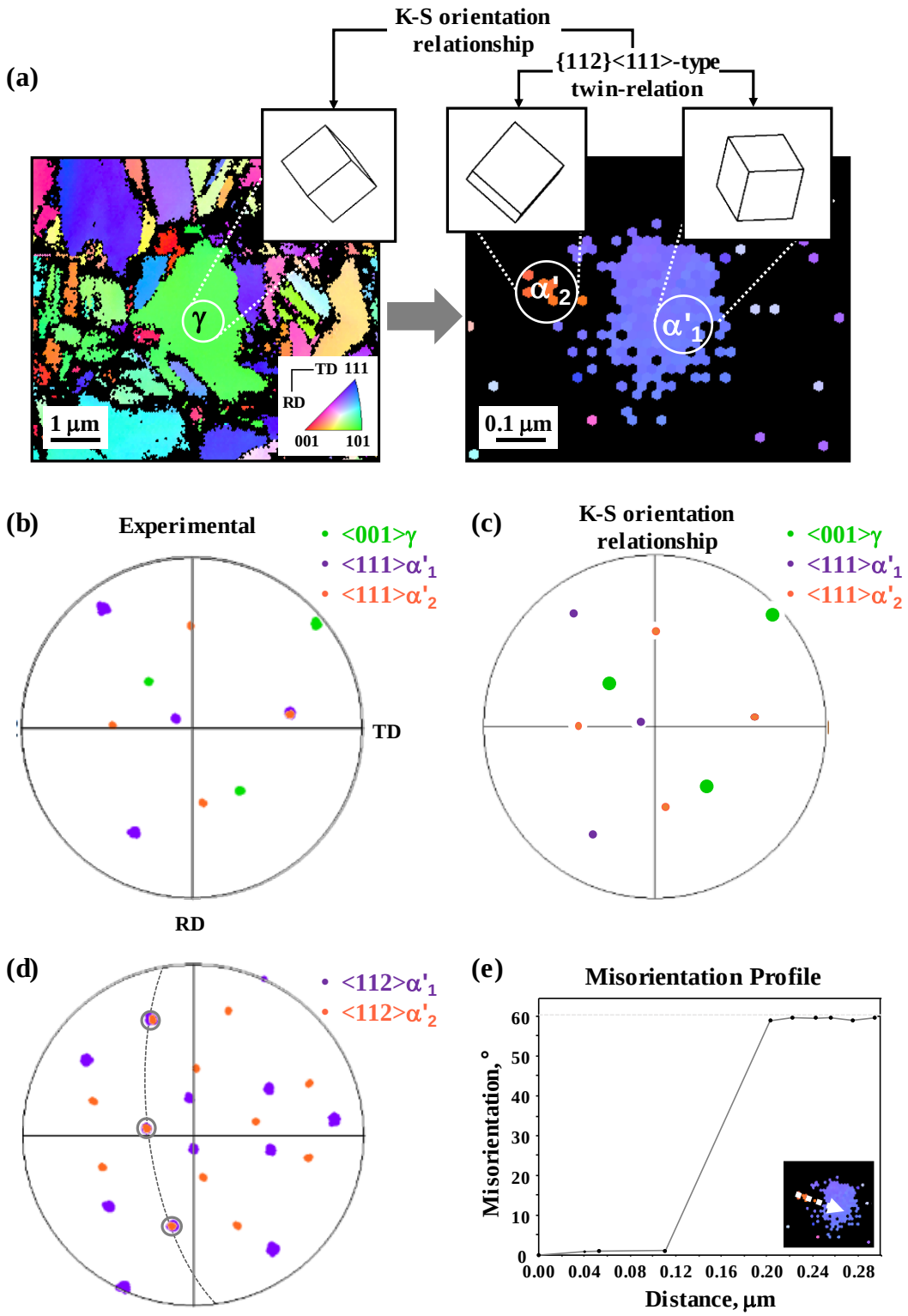


Supplementary Fig. S1. Crystallographic orientation data of the top surface of the quenched and partitioned (Q&P) steel micro-pillar shown in Fig. 3 before the focused ion beam (FIB)

scanning and after the micro-pillar fabrication. (a) Electron backscatter diffraction (EBSD) inverse pole figure (IPF) maps for the retained austenite (FCC) and martensite (BCC) and three-dimensional crystal orientations, represented by unit cells, for the parent retained austenite (left) and two product martensite variants formed due to the $Ga^+$ ion beam damage (right). (b) <001>γ pole figures of the retained austenite and <111>α' pole figures of the product martensite variants. (c) Simulation of the theoretical <111>α' pole figures for two of the 24 possible Kurdjumov-Sachs (K-S) variants closely matching the experimental pole figures. (d) <112>α' pole figures for the two martensite variants showing the coincidence of the three <112>α' poles (marked by grey circles) lying on the plane trace for the common <111>α' axis. (e) Misorientation profile of the investigated twinned martensite, taken across the twin boundary, as indicated by the dashed arrow in the inset. γ and α' represent the retained austenite and martensite, respectively.